Catalytic nickel nanoparticles embedded on ZIF-8 backbone for accelerating polysulfide conversion in lithium-sulfur batteries

Jixin Lu [a,b], Mengyuan Zhu [b], MinSu Kim [c], Aihua He [b], Cunguo Wang [b,*] , Tae Hyung Kim [c,**], Seung Hee Lee [a,c,d,***]

[a] Department of JBNU-KIST Industry-Academia Convergence Research, Jeonbuk National University, Jeonju, 54896, Republic of Korea
[b] Shandong Key Laboratory of High Performance Polyolefin Materials and Recycling, State Key Laboratory of Advanced Optical Polymer and Manufacturing Technology, Qingdao University of Science and Technology, Qingdao, Shandong 266042, China
[c] Department of Nano Convergence Engineering, Jeonbuk National University, Jeonju, 54896, Republic of Korea
[d] Department of Polymer-Nano Science and Technology, Jeonbuk National University, Jeonju, 54896, Republic of Korea

HIGHLIGHTS

- Ni-nanoparticles-embedded nitrogen-rich porous carbon synthesized for Li-S battery.
- Ni-CN exhibits superior conductivity, high surface area, and substantial porosity.
- Ni-CN cathodes promote polysulfide conversion and suppress the shuttle effect.
- Sulfur-loaded Ni-CN-based cathodes facilitate efficient kinetic conversion.
- A maximum discharge specific capacity of 1295.3 mAh/g at 0.1 C was realized.

ARTICLE INFO

ABSTRACT

Lithium-sulfur batteries (LSBs) are considered one of the most promising next-generation energy storage systems owing to their ultrahigh energy density and discharge-specific capacity. However, the poor conductivity of active sulfur and the shuttle effect caused by lithium polysulfides (LiPSs) lead to a rapid decrease in the charge and discharge capacities of batteries, seriously hindering their further development. In this study, metallic nickel nanoparticles are successfully introduced into a nitrogen-rich porous carbon framework (Ni-CN) material using a solvothermal method. The addition of metallic nickel improves the adsorption and conversion ability of the CN towards polysulfides, thereby improving the reaction kinetics. The symmetrical battery assembled with Ni-CN exhibits a higher current response, indicating that the nickel nanoparticle catalyst has excellent catalytic ability. The results indicate that the battery assembled with sulfur-loaded Ni-CN (S@Ni-CN) has excellent cycling performance, with a maximum discharge specific capacity of 1295.3 mAh/g at 0.1C and a discharge specific capacity of 906.7 mAh/g after 200 cycles, with an average capacity decay of about 0.15 % per cycle. In contrast with traditional porous carbon electrodes, Ni-CN demonstrates superior adsorption capacity for polysulfides and enhances the conversion rate of these compounds, leading to a more efficient utilization of sulfur.

1. Introduction

Compared to lithium-ion batteries, lithium-sulfur batteries have the advantages of high energy density (2600 Wh/kg), environmental friendliness, and low cost, making them one of the most promising candidates for the next generation [1–3]. Although lithium-sulfur batteries have the above advantages, there are some limitations in their development, such as the poor electrical conductivity of singlet sulfur and its discharge products (Li_2S_2 and Li_2S), the serious volume expansion phenomenon during charging and discharging, and the shuttle

effect caused by the dissolution and migration of polysulfides during the reaction process [4–6].

Researchers have proposed many strategies for addressing these problems. The most prominent approach is the introduction of porous carbon materials such as carbon nanotubes, graphene, and porous carbon [7–13]. Although these materials exhibit excellent electrical conductivities, they bind poorly to polar polysulfides because of their weak physical interactions and cannot effectively inhibit the shuttling effect. In this case, researchers introduced heteroatoms (e.g., nitrogen (N), phosphorus, oxygen (O), and halogenated elements) into cathode materials to improve the adsorption of polysulfides [14–18]. However, the binding ability of nonmetallic element-doped carbon to polysulfides is limited, and the binding energy is generally less than 1.5 eV [19]. In contrast, some metal compounds (e.g., MoS_2 and TiO_2) have a stronger binding ability to polysulfides [20,21], which can improve the cycling stability of the batteries to a certain extent. However, the electrical conductivity of these metal compounds is generally poor, which could potentially slow the redox kinetics of the LSB [22,23]. Furthermore, the analysis of the results revealed that enhancing the transformation of LiPSs was crucial in reducing the shuttle effect. Nonetheless, the mere introduction of heteroatoms and enhancement of the mechanical stability of the cathode material is inadequate for achieving a rapid conversion of polysulfides.

In general, carbon materials with high pore volumes, excellent electrical conductivities, and adjustable structures are often considered ideal sulfur host materials [24–26], and the characteristics of metal-organic framework (MOF)-based materials are in line with those mentioned above, which have attracted much attention from researchers [27–34]. It has been shown that MOF-based materials, after high-temperature cracking, not only have excellent electrical conductivity but also have a strong adsorption capacity for polysulfides with high heteroatom content [35–38]. In addition, it has been reported that metals such as iron, cobalt, and nickel (Ni) exhibit significant catalytic activity toward the redox reaction of LSBs, which can significantly accelerate the conversion reaction kinetics of LiPSs and exert an anchoring effect on polysulfides. Recent studies have also demonstrated that transition metal-based compounds, such as Ni/Fe-based nanomaterials, have excellent electrocatalytic activity toward water splitting reactions, due to their favorable electronic structures and abundant active sites [39,40]. These findings suggest that similar transition metal-based catalysts may also exhibit high activity in Li–S systems by accelerating polysulfide conversion and lithium sulfide decomposition [41]. He and the co-worker group verified through theoretical calculations that the d-orbital electrons of transition metals are capable of hybridizing with the p-orbital electrons of polysulfides and change their electronic structure, thereby accelerating the conversion process between polysulfides and reducing the decomposition energy barrier of lithium sulfide. This also proves that transition metals have a significant catalytic effect on the redox reactions during charge and discharge processes [42]. In addition, the conductivity and effective utilization rate of the transition catalyst itself also need to be considered. Xie and co-workers combined $Co_{0.85}Se$ nanoparticles with porous carbon materials, significantly improving the conversion rate of polysulfides [43].

In this study, we successfully composited Ni catalysts into zeolitic imidazole framework (ZIF) using a solvothermal method. After high-temperature carbonization, Ni nanoparticles were uniformly distributed in the nitrogen-rich carbon framework (CN) and applied as sulfur-based skeleton materials in LSBs. The porous structure of CN effectively inhibits the aggregation of nickel nanoparticles, resulting in the formation of uniformly distributed 10 nm nickel metal particles within the porous carbon matrix. This uncovers further catalytic sites for nickel and increases the interaction surface between the nickel catalyst and polysulfide, improving reaction activity and efficiency in experimental settings. The material has the following advantages. (1) The as-prepared Ni-CN composite material is ultralight and porous, which can realize high sulfur loading and effectively reduce the impact on the mechanical

stability of the electrode due to volume changes. (2) Ni not only synergistically anchors the soluble LiPSs with N atoms but also enhances the redox reaction kinetics of LiPSs. (3) Its porous conductive shell layer facilitates the enhancement of the lithium ion and electron transfer rates and the reactivity of sulfide. After electrochemical performance testing, the battery exhibited an initial discharge-specific capacity of 1288.6 mAh/g at a rate of 0.1C. Even after 200 extended cycles, the reversible capacity of the battery remained at 906.7 mAh/g, resulting in a capacity retention rate of 70.4 %. Furthermore, the average capacity degradation rate for each cycle is only 0.15 %.

2. Experimental

2.1. Materials

Zinc nitrate hexahydrate ($Zn(NO_3)_2 \cdot 6H_2O$, ≥99.5 %), 2-methylimidazole (≥99.5 %), N-methyl-2-pyrrolidinone (≥99.9 %), nickel acetate (≥99 %), sulfur (≥99.9 %), and lithium sulfide (≥99.9 %) were all purchased from Aladdin Scientific (China). Methanol was purchased from the China National Pharmaceutical Group (China). PVDF was purchased from the Arkema (France). 1,2-Dimethoxyethane (DME) and 1,3-dioxolane (DOL) were obtained from DodoChem (China).

2.2. Synthesis of Ni/ZIF-8 and ZIF-8

In this study, the preparation method of the ZIF-8 materials was modified from that reported in the literature [44]. First, 3.284 g of 2-methylimidazole was added to 60 mL of methanol and stirred thoroughly to ensure complete dissolution. Then 2.3799 g of $Zn(NO_3)_2 \cdot 6H_2O$ and 0.1766 g of nickel acetate were dissolved in another 60 mL of methanol, and the two solutions were mixed and sonicated for 20 min in an ultrasonicator. Subsequently, the mixed solution was stirred for 1 h and then reacted in a PTFE-lined autoclave reactor at 120 °C for 4 h. After natural cooling, the mixture was centrifuged. The precipitate was removed and rinsed multiple times with methanol, the Ni/ZIF-8 was obtained after complete drying. The preparation of ZIF-8 material was basically the same as that of Ni/ZIF-8, except that nickel acetate was not added to the solution.

2.3. Synthesis of Ni-CN and CN

The above-obtained Ni-ZIF-8 was ground thoroughly and then transferred to a tube furnace and heated at 3 °C/min to 930 °C for 3 h under an N_2 atmosphere. After natural cooling, a black powder-like product, Ni–CN, was obtained. The preparation process for CN was the same as that for Ni-CN, except that the precursor material was changed to ZIF-8. The remaining steps were identical to those used for the preparation of Ni-CN.

2.4. Preparation of sulfur loading in Ni-CN and CN

The sulfur-loaded Ni-CN (S@Ni-CN) was obtained by mixing and grinding sulfur and Ni-CN at a mass ratio of 7:3 and subsequently heating in a reactor at 155 °C for 12 h to fully penetrate sulfur into the Ni-CN skeleton. The synthesis of S@CN was similar to that of S@Ni-CN, except that CN was used.

2.5. Material characterization

Morphological characterization of the samples was carried out using field-emission scanning electron microscopy (FE-SEM, Regulus 8100, Japan) and transmission electron microscopy (TEM, JEM-ARM200F, Japan). Brunauer–Emmett–Teller (BET) measurements of the pore size distribution and specific surface area were performed using a surface area and pore size analyzer (ASIQA 3501–5, USA). The sulfur content was determined using a thermogravimetric (TG) analyzer (Q500, USA).

Fourier transform infrared (FTIR) was used to analyze the chemical bonds and molecular composition of materials (Nicolet Is20, Thermo Scientific, USA). Powder X-ray diffraction (XRD) was conducted utilizing an X-ray diffractometer (Ultima IV, Japan). The analysis of the chemical composition and bonding of the resulting materials was conducted utilizing X-ray photoelectron spectroscopy (XPS; Theta Probe instrument, Thermo Fisher Scientific, UK).

2.6. Electrode fabrication

S@Ni-CN, carbon black, and polyvinylidene fluoride were weighed at a mass ratio of 7:2:1, fully ground in a mortar, added to an appropriate amount of N-methyl-2-pyrrolidinone (NMP) solution, and stirred for 12 h. The S@Ni-CN electrode slurry was uniformly coated on clean aluminum foil using a spatula and placed in a vacuum drying oven at 60 °C for 12 h. A cell slicer was employed to punch a 13 mm diameter disc so that the sulfur loading on the cathode was about 1.7–2.5 mg/cm^2.

2.7. Cells fabrication

The CR2032 coin cell was assembled entirely within a glove box filled with high-purity argon atmosphere in which the oxygen and moisture contents were less than 0.1 ppm. A polyethylene membrane (Celgard 2400) was used as the separator, and the electrolyte was 1.0 M LiTFSI dissolved in DOL/DME (v/v = 1:1 + 2.0 wt% LiNO$_3$).
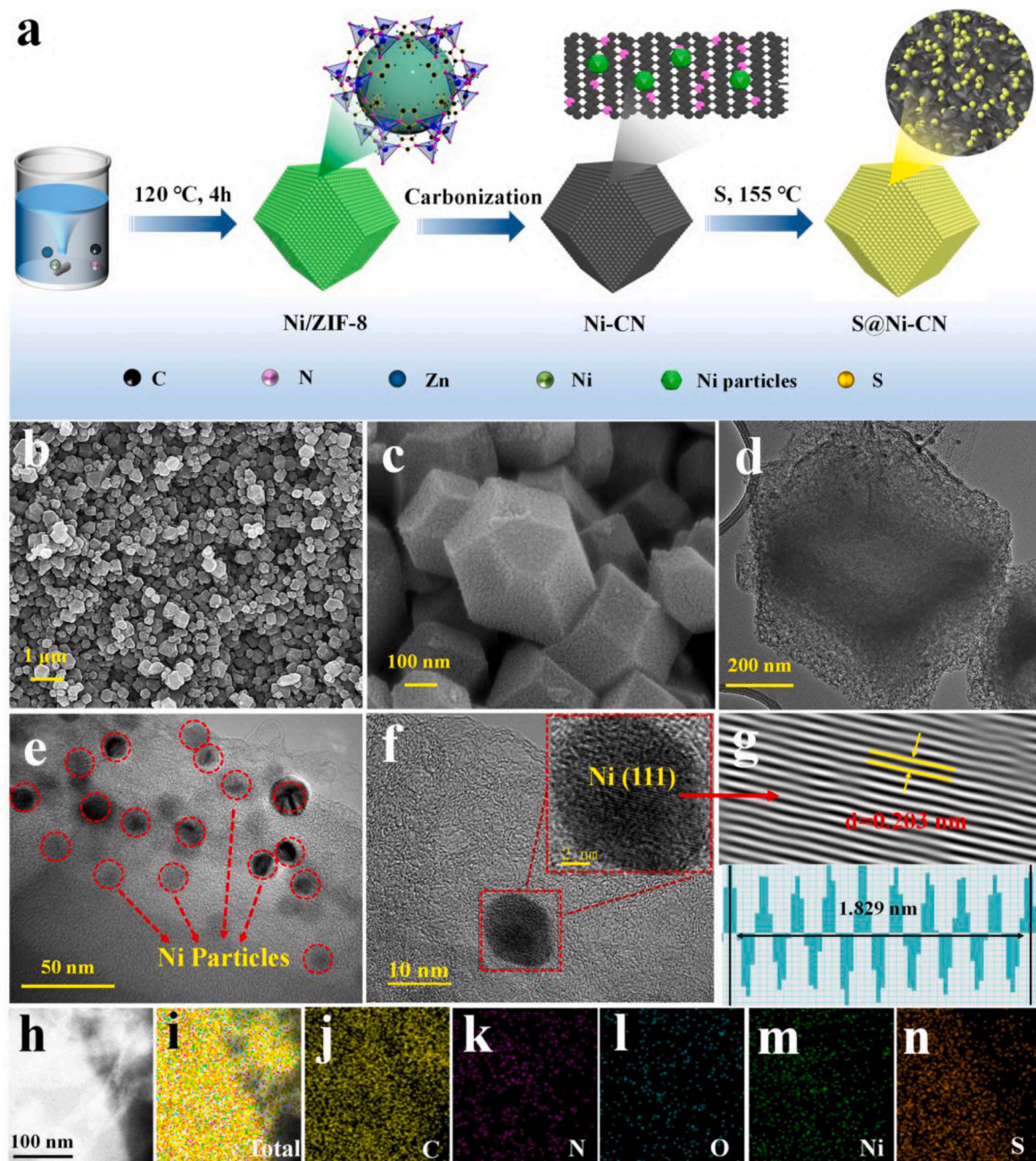
Fig. 1. (a) Schematic diagram of the S@Ni-CN synthesis process. (b, c) SEM images of Ni-CN at different magnifications. (d, e) TEM images of Ni-CN at different magnifications. (f) HR-TEM images of Ni-CN and (g) the IFFT pattern with line profile of d-spacing from Fig. 1f. (h) HAADF-STEM images of S@Ni-CN. EDS color mapping of the S@Ni-CN. (i) Overall mapping elements, (j) carbon, (k) nitrogen, (l) oxygen, (m) nickel, and (n) sulfur. (For interpretation of the references to color in this figure legend, the reader is referred to the Web version of this article.)

2.8. Electrochemical measurements

Celgard 2400 membrane and lithium foil were used as a separator and anode, respectively. The electrolyte comprised 1 M lithium bis(tri-fluoromethanesulfonyl)imide (LiTFSI) and 0.1 M $LiNO_3$ dissolved in a solution of DOL and DME (v/v = 1:1). The cyclic voltammetry (CV) curves and rate performance were evaluated within a 1.5–2.8 V voltage range, employing a Chi760e electrochemical workstation. The discharge-charge tests were conducted within the voltage range from 1.5 to 2.8 V on a Land Testing System. The electrochemical impedance spectroscopy (EIS) spectra were analyzed utilizing the Chi760e electrochemical workstation across a frequency range of 0.01 Hz–0.1 MHz.

3. Results and discussion

3.1. Structural characterization

The synthesis process of S@Ni-CN is shown in Fig. 1, in which Ni/ZIF-8 was first synthesized by the solvothermal method, followed by its high-temperature carbonization at 930 °C. Finally, sulfur was introduced into the backbone material via melt diffusion. XRD was used to analyze the structure of the prepared materials. ZIF-8 and Ni/ZIF-8 exhibited higher crystallinity and similar crystal structures (Fig. S1). The Fourier transform infrared (FTIR) spectra were used to compare the composition of Ni/ZiF-8 and ZIF-8 before carbonization (Fig. S2). The characteristic peaks at 995 and 1425 cm^{-1} indicate the stretching vibrations of C–N. Concurrently, due to the stretching vibration of the –CN group, a small absorption peak appears at 1584 cm^{-1}. In addition, a significant absorption peak appeared at 3450 cm^{-1}, which was caused by the stretching vibration of O–H. The presence of the basic characteristic peak of ZIF-8 confirmed the successful synthesis of Ni-doped ZIF-8.

The structure and morphology of Ni-CN were studied by FE-SEM and TEM. The FE-SEM images of the Ni-CN material with different magnifications (Fig. 1b–c) demonstrate that the product after high-temperature cleavage still maintains a relatively regular rhombic polyhedral structure, with the diameter of the Ni-CN particles being

approximately 400 nm. The FE-SEM image of CN shows a structure similar to Ni-CN, both retaining a regular polyhedral structure. The TEM images in Fig. 1d–e shows the microstructures of Ni-CN and CN. A thin layer of carbon formed on the surface of the carbonized ZIF-8, which helped limit the overflow of LiPSs. The microstructures of CN and Ni-CN are similar (Fig. S4). In addition, nickel nanoparticles with a diameter of approximately 10 nm are uniformly distributed within the carbon material and exhibit a favorable crystalline state as shown in Fig. 1f. The Inverse Fast Fourier Transform (IFFT) and line profile of d-spacing with 0.203 nm of Ni nanoparticles are shown in Fig. 1g, which is consistent with the XRD data for Ni-CN. The high-angle annular dark field scanning transmittance electron microscopy (HAADF-STEM) image of S@Ni-CN (Fig. 1h) and the corresponding energy dispersive X-ray spectroscopy (EDS) analysis (Fig. 1i–n) show that carbon, N, O, Ni, and sulfur are uniformly distributed, indicating the successful synthesis of S@Ni-CN composite materials, which is conducive to charge transfer and advances the utilization efficiency of the sulfur.

The crystallinities of CN and Ni-CN were analyzed by XRD (Fig. 2a). It can be seen from the figure that Ni-CN exhibits peaks at 25°, 44°, 52°, and 76°, corresponding to the (002) characteristic crystal plane of the carbon and the characteristic crystal planes of Ni (111), (200), and (220), respectively. This further demonstrates the successful introduction of Ni metal catalysts [45,46], and indicates that the material exhibited a high degree of graphitization after carbonization. The pore structures of the CN and Ni-CN were characterized using N_2 adsorption/desorption isotherms. According to Fig. 2b, the adsorption–desorption curves of the two materials belong to the I-type isotherm, which indicates that both materials are microporous carbon materials that correspond to the pore size distribution curves of the materials. The specific surface area of CN was 2211.424 m^2/g and the pore volume was 1.381 cm^3/g, as calculated using the BET theory. In comparison, the Ni-CN material had a specific surface area of 2556.847 m^2/g and a pore volume of 1.632 cm^3/g. Fig. 2c shows the test curves for pore size distribution of CN and Ni-CN, from which it is evident that the pore sizes of both materials are mainly concentrated between 1.0 and 2.5 nm, with the average pore diameter of CN being about 1.6 nm and that of Ni-CN being 1.9 nm. Compared with lithium ions (~1.52 Å) and
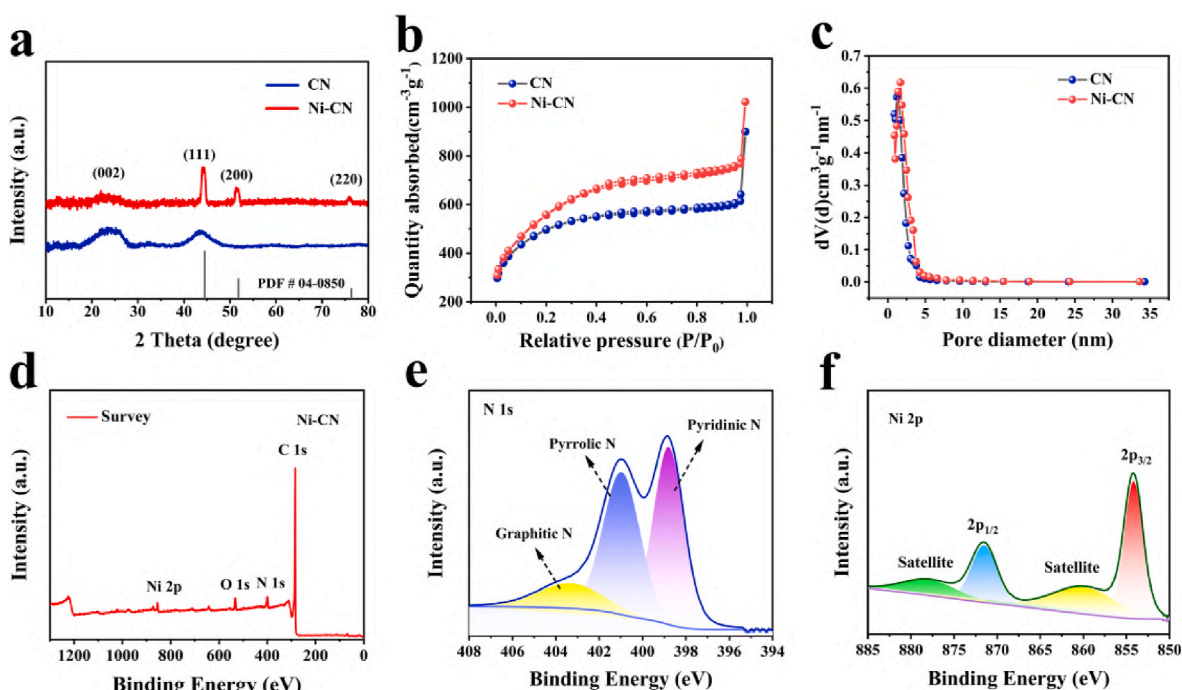
Fig. 2. (a) XRD patterns of Ni-CN and CN. (b) Nitrogen adsorption and desorption curves of CN and Ni-CN. (c) Pore size distribution of CN and Ni-CN. (d) Survey XPS spectrum and high-resolution XPS spectra of (e) N 1s and (f) Ni 2p for the Ni-CN.

polysulfides (~7.9 Å), the pore sizes of both materials are sufficiently large to allow them to enter and exit quickly and freely. These results show that heat treatment of Ni/ZIF-8 at 930 °C removes zinc and other small organic molecules from the inside of the material and forms a rich pore structure that allows the electrolyte to enter the interior of the Ni-CN material, thereby increasing the contact area with the active material. This indicates that sulfur utilization can be improved by increasing and promoting lithium-ion transport.

XPS is a powerful tool for examining chemical states on the surface of a material. Fig. 2d shows the survey spectrum of Ni-CN, demonstrating the inclusion of the nickel, oxygen, nitrogen, and carbon. The deconvolution of the N 1s spectra demonstrated three binding energy peaks at approximately 398.6, 400.8, and 403.3 eV, corresponding to pyridinic, pyrrolic, and graphitic nitrogen, respectively (Fig. 2e) [47]. The N doping of the carbon matrix can reach up to 6 %, which promotes the adsorption and conversion kinetics of LiPSs, thereby limiting the shuttle effect [48]. Analysis of the Ni 2p spectrum through peak deconvolution indicates two distinct contributions situated around 854.5 and 872.2 eV, which are attributed to the Ni $2p_{3/2}$ and Ni $2p_{1/2}$ spin–orbit components. Two broad peaks located at approximately 860.5 and 878.6 eV represent satellite peaks (Fig. 2f) [49]. The deconvolution of the C 1s spectrum exhibited three distinct peaks centered at binding energies of 284.8, 286.1, and 288.9 eV representing C–C, C–N, and C–O bonds, respectively (Fig. S5a). The deconvolution of the O 1s spectrum revealed two peaks at approximately 531.7 and 533.6 eV, corresponding to oxygen in C–O and C=O bonds, respectively (Fig. S5b) [50].

The adsorption capacity of polysulfides is a crucial factor in evaluating the performance of host materials for LSBs. The strong adsorption capacities of various host materials for polysulfides were confirmed through visual experiments (Fig. S6). Certain amounts of Ni-CN and CN materials were placed in a sealed small bottle containing as-prepared 0.2 M Li_2S_6 solution. Following 6 h, the solution with Ni-CN became colorless, demonstrating its higher capture ability and affinity for LiPSs compared to CN. After the adsorption test was completed, the solution was diluted to a certain concentration, and ultraviolet (UV) measurements were performed. The characteristic peak of Li_2S_6 appeared at

approximately 270 nm, and the blank Li_2S_6 solution exhibited a higher absorption intensity at this wavelength (Fig. S6). In contrast, the solution with Ni-CN exhibited weak absorption intensity, indicating its high anchoring ability for LiPSs.

The samples were gathered for subsequent XPS analysis following the adsorption tests. The survey spectrum of Ni-CN revealed the existence of nickel, oxygen, nitrogen, sulfur, and carbon (see Fig. S7). The Li–O bond appeared at a binding energy of 530.8 eV, which explains the interaction between the Li and O atoms after the Li_2S_6 adsorption (Fig. S8a) [51]. The S 2p spectrum was deconvoluted into two peaks at binding energies of 163.9 and 168.5 eV, which correspond to S^{2-} $2p_{3/2}$ and S^{2-} $2p_{1/2}$, respectively (Fig. S8b) [50]. A noticeable movement of the Ni 2p fine scan to higher binding energies was seen, which is attributed to the increased electron density on Ni induced by its stronger interaction with S compared to Ni–CN (Fig. S9). A thermogravimetric test was conducted to measure the S weight in the S@Ni-CN composite materials (Fig. S10). When the experimental temperature was raised from room temperature to around 400 °C, the weight loss rate of the composite material reached 72 %. This indicated that the weight ratio of S in the host materials was 72 %.

3.2. Electrochemical performance

To analyze the catalytic capabilities of Ni-CN and CN electrode materials for polysulfide conversion reactions, we assembled symmetric cells using 0.2 M Li_2S_6 dissolved in DOL/DME electrolyte (v/v = 1/1). The test results are shown in Fig. 3a. We can observe different peaks in the CV curve of the symmetrical battery, labeled as A, B, C, and D. Different peaks represent different redox reaction processes (Peak A and peak D: $4S_6^{2-} \leftrightarrow 3S_8 + 8e^-$; Peak B and peak C: $S_6^{2-} + 10e + 12Li^+ \leftrightarrow 6Li_2S$). Compared to the CN electrode, the CV curve of Ni-CN exhibited a higher reaction current, suggesting a notable enhancement in the conversion kinetics of polysulfide. This indicates the significant catalytic efficiency of the Ni-CN electrode in the liquid–solid conversion process. Subsequently, cyclic stability tests were conducted on symmetric batteries assembled from the two materials at 20 mV/s. The Ni-CN-based
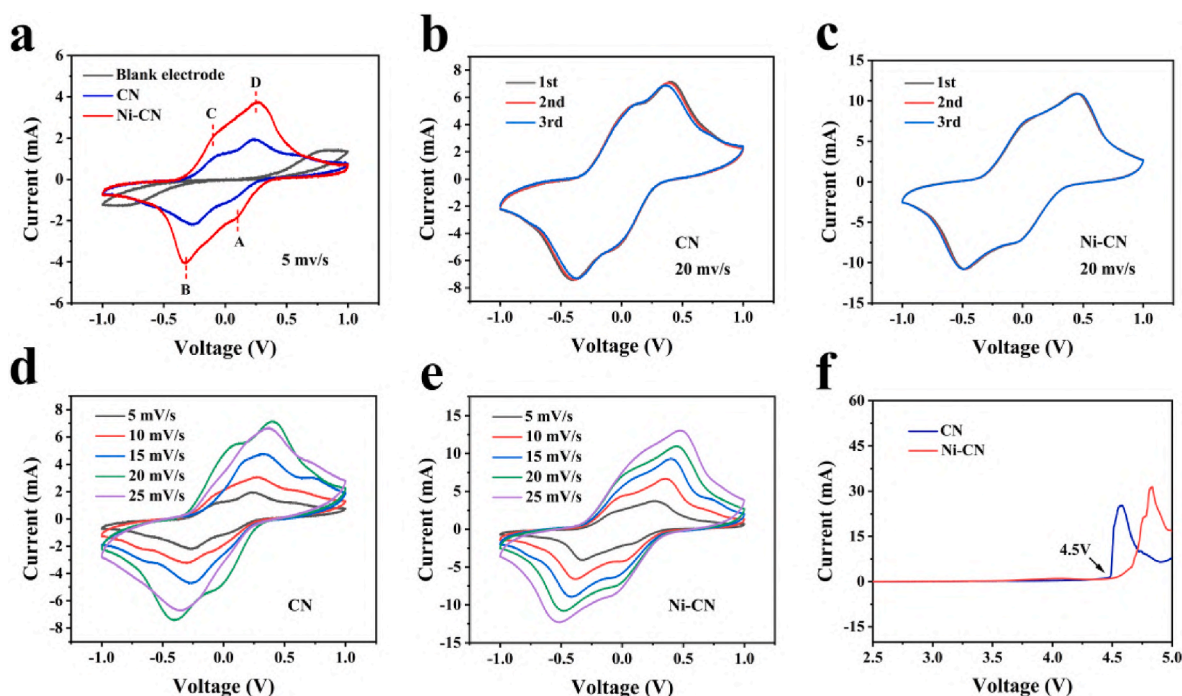
Fig. 3. (a) Cyclic voltammetry (CV) curves of symmetric cells based on different sulfur hosts. CV curves of the Li_2S_6 symmetrical batteries with (b) CN and (c) Ni-CN at a scan rate of 20 mV/s (d) CV curves of Li_2S_6 symmetric batteries with CN at different scan rate. (e) CV curves of Li_2S_6 symmetric batteries with Ni-CN at different scan rates. (f) Linear sweep voltammetry curves for CN and Ni-CN.

symmetric battery exhibited better cyclic stability, as shown in Fig. 3b and c. The CV curves of the CN and Ni-CN symmetric cells at different scanning rates, as shown in Fig. 3d and e. It was found that at different scanning rates, compared to the CN, symmetric cells assembled with Ni-CN exhibited higher reaction currents. This also indicates that the introduction of the Ni catalyst significantly improved the reaction activity for polysulfide conversion.

The electrochemical stability of CN and Ni-CN materials was analyzed using linear sweep voltammetry (LSV) at 0.5 mV/s within the voltage range of 2.5–5 V (Fig. 3f). Before 4.5 V, both materials exhibited significant current fluctuations. When the voltage was increased to 4.5 V, the electrolyte decomposed, and the CN electrode material first showed a significant change in current, indicating that Ni-CN had better chemical stability. In general, the transition from Li_2S_4 to Li_2S constitutes three-quarters of the theoretical battery capacity. Therefore, fast and uniform Li_2S nucleation is important for improving battery performance [52,53]. To test the effect of Ni-CN on the transformation of polysulfides, we conducted nucleation tests on Li_2S. The electrodes were produced by casting sulfur/host material on aluminum foil (S loading = 0.4 mg/cm^2), and using lithium as the anode of the battery, LSB electrolyte is added to both the cathode and anode sides during battery assembly. First, the battery was discharged to 2.07 V, it was then changed to discharge at 2.06 V, and the change in current was recorded. The cell with the Ni-CN cathode demonstrated enhanced deposition capacity of 114.12 mAh/g, which performs better than that of the battery with CN cathode (109.77 mAh/g), as observed in Fig. 4a and b. Moreover, the cell with the Ni-CN displayed a more distinct peak during the shorter time (503 s). This result confirms that Ni nanoparticles can accelerate

the conversion reaction rate of LiPSs and improve the specific capacity of LSB. In addition, the kinetics were examined through a Li_2S decomposition test. (Fig. 4c and d). The Ni-CN cathode exhibited a higher peak current compared to the CN cathode, suggesting that the overpotential necessary for the dissolution of Li_2S was reduced. [54,55]. Moreover, the capacity for Li_2S decomposition on Ni-CN was high (462.69 mAh/g), which is superior to CN (428.37 mAh/g). This indicates that anchoring of Ni nanoparticles in the CN can improve the oxidation reaction kinetics of Li_2S.

Fig. 5a shows the mechanism by which the assembled LSB enhanced the electrochemical performance. The addition of Ni nanoparticles enhances the transformation of carrier materials into LiPSs and reduce their dissolution concentration in the electrolyte. In contrast, nitrogen-rich porous structures provide effective pathways for lithium-ion diffusion. To verify the electrochemical performances of the different electrodes, a lithium metal anode was used to assemble the batteries for CV testing. As observed in Fig. 5b, an obvious oxidation peak appeared at 2.34 V in the S@Ni-CN battery, corresponding to the transformation of Li_2S to S. Moreover, two reduction peaks were observed at 2.32 V and 2.0 V, corresponding to the sulfur to LiPSs and LiPSs to Li_2S conversion processes, respectively. In contrast, the CV curve of S@CN showed a weaker peak intensity and varying degrees of shift. Fig. 5c shows that the S@Ni-CN has a higher peak current, which indicates that the S@Ni-CN has a lower degree of polarization and faster redox kinetics.

Fig. 5d–f shown local magnifications of the CV curves of S@CN and S@Ni-CN. As seen in the graph, the S@Ni-CN has a lower initial reaction potential, indicating its higher reaction activity. The Tafel curve is shown in Fig. 5g–i, which are used to examine the catalytic properties of
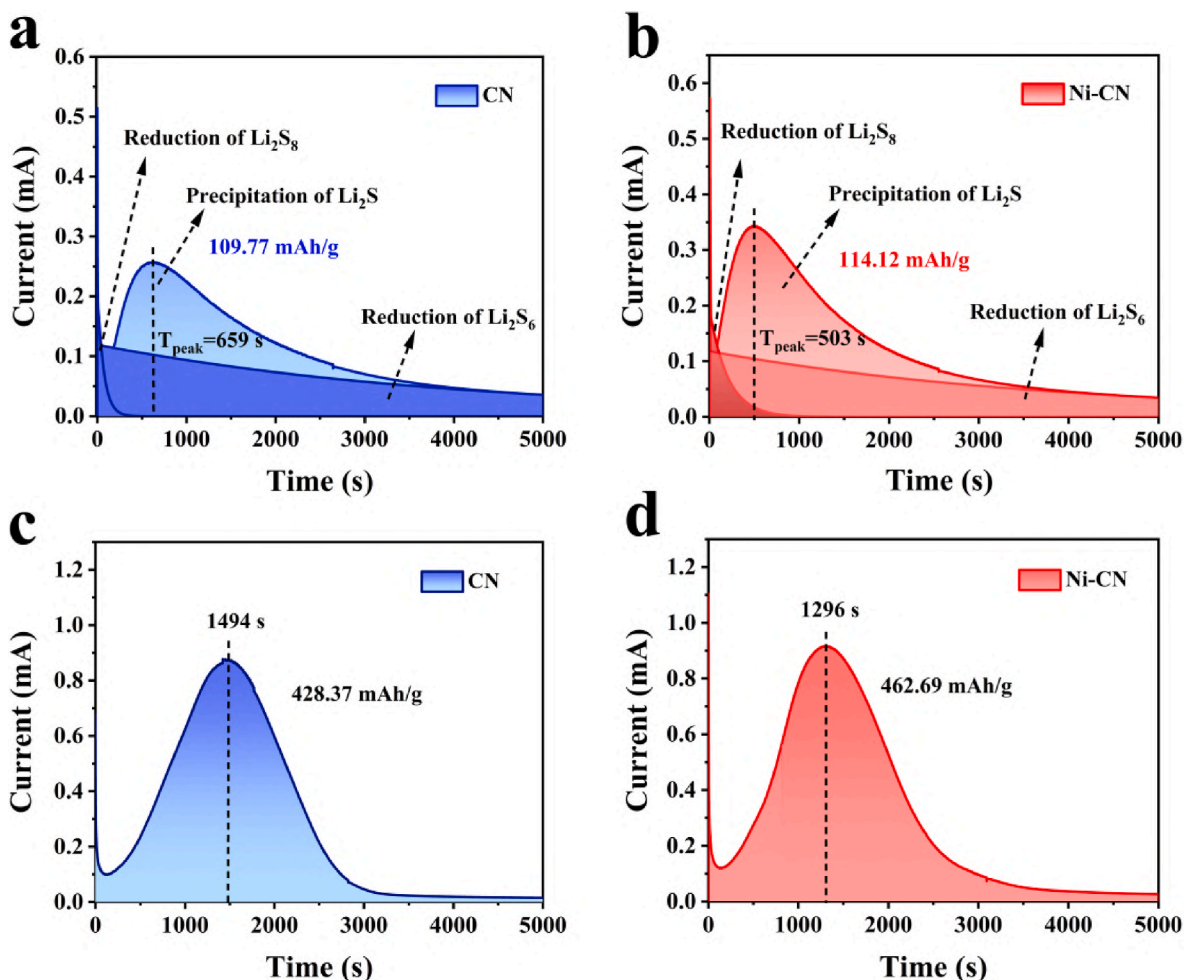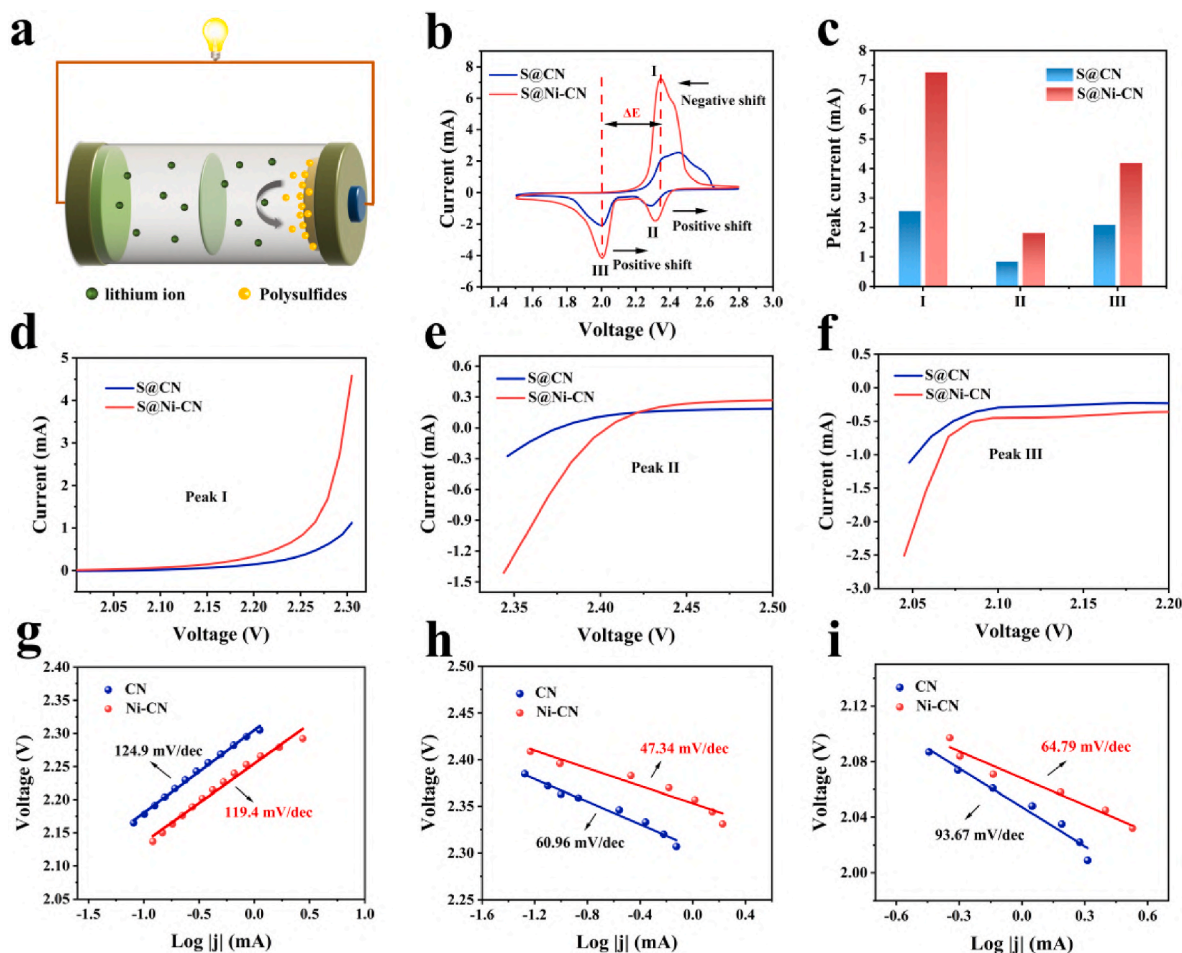

Fig. 4. Li_2S nucleation curves on (a) CN and (b) Ni-CN at 2.05 V Li_2S decomposition curves on (c) CN and (d) Ni-CN at 2.4 V.

Fig. 5. (a) Schematic illustration of the synergistic adsorption-catalytic effect of Ni-CN on polysulfides. (b) CV curves of S@CN and S@Ni-CN electrodes at 0.1 mV/s. (c) Peak current of CV curves for different electrodes. Enlarged local images of CV curves: (d) oxidation peak I, (e) reduction peak II, and (f) reduction peak III. Tafel plots of (g) oxidation peak I, (h) reduction peak II, and (i) reduction peak III.

the carrier material in the redox transformation of polysulfides. The fitting slopes of the oxidation peak I and reduction peaks II and III of the Ni-CN electrodes are 119.4, 47.34, and 64.79 mV/dec, respectively, which are much smaller than the fitting slopes of the CN-based electrode (124.9, 60.96, and 93.67 mV/dec), indicating that through the collaborative action of N-rich porous structure physical and chemical adsorption and Ni catalyst, lithium polysulfide can be rapidly converted.

The transfer rates of electrons and ions on different electrodes were analyzed using electrochemical impedance and CV tests. Fig. 6a shows the electrochemical impedance spectroscopy (EIS) curves and corresponding circuit impedance simulations of the S@CN and S@Ni-CN. The EIS curve shows a semicircle at high frequencies and a straight line at low frequencies, which correspond to the charge transfer resistance (R_{ct}) and ion diffusion resistance (R_0) of the electrode material, respectively. From the figure, it can be seen that the R_{ct} and R_0 of the S@CN material are approximately 51.4 Ω and 16.53 Ω, respectively. In contrast, the S@Ni-CN material has a smaller semi-circular diameter, indicating a smaller R_{ct} (35.36 Ω) and ion diffusion resistance (8.27 Ω). This indicates that the introduction of electron-rich Ni catalysts reduces the R_{ct} of the material, enhances the transport efficiency of ions and promotes the redox reaction.

The diffusion coefficient of lithium ions can intuitively reflect the reaction rate of the electroactive species; the larger its value, the greater the conversion rate of lithium polysulfides. CV tests were conducted on the S@CN and S@Ni-CN at different scanning rates to determine the effect of the Ni catalyst on the kinetics of the electrode redox reaction. Fig. 6b and c displays the CV curves for S@CN and S@Ni-CN at various

scanning rates, with the peak currents for the oxidation peak marked as I_A and the peak currents for the reduction peaks marked as I_{C1} and I_{C2}. The graph shows that the peak currents of both electrodes increased along with the rising. Compared to the S@CN, the S@Ni-CN exhibited a higher peak current. According to the Randles–Sevcik equation [52,56].

$$I_P = (2.69 \times 10^5) n^{1.5} S D_{Li}^{+0.5} \Delta C_{Li} \nu^{0.5}. \tag{1}$$

In this equation, I_P and ν denote the corresponding peak current and scan rate in the CV curve, respectively. Because the electron transfer number n, the geometrical area S of the sulfur cathode, and the lithium-ion concentration C_{Li} are all constant values, the peak current (I_A) of the oxidation peak (A) and the peak currents (I_{C1}, I_{C2}) of the reduction peaks ($C1$, $C2$) are linearly dependent on the square root of the scanning rate, and the lithium-ion diffusion rate (D_{Li}^+) of the S@CN and S@Ni-CN were determined from the slopes of the fitted lines ($I/\nu^{0.5}$). As shown in Fig. 6d–f, according to the slopes of the fitted lines obtained within the graph, the lithium-ion diffusion rates of all peaks of S@Ni-CN were significantly higher than those of the cell based on S@CN, demonstrating that the addition of the Ni catalyst can accelerate the lithium-ion transport rate and enable the cell to have higher lithium-ion fluxes, which promotes the migration of electrons and the conversion of polysulfides to enable the LSB to obtain a more stable long-cycle performance. In addition, the high overlap of the CV curves during the charging/discharging processes indicates that the S@Ni-CN shows excellent electrochemical reversibility (Fig. S11). To further analyze the effects of different materials on the decomposition of lithium sulfide, we conducted additional galvanostatic intermittent titration technique
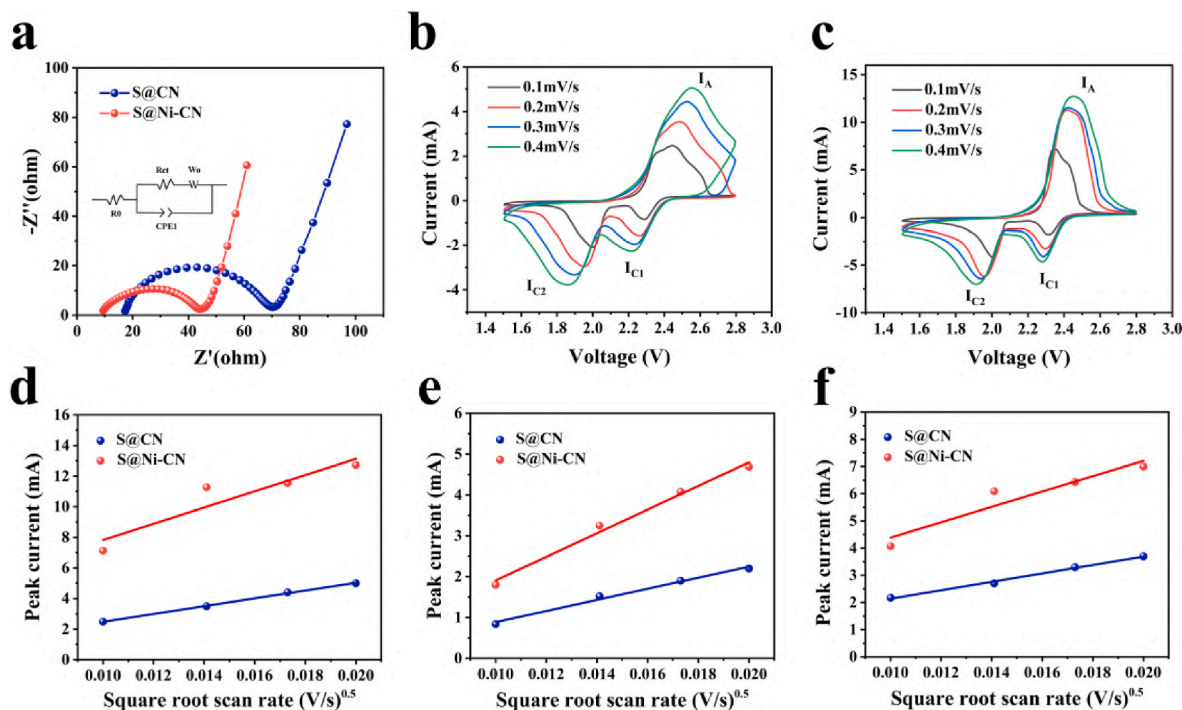
Fig. 6. (a) EIS curves of S@CN and S@Ni-CN electrodes. The CV curves of (b) S@CN and (c) S@Ni-CN at 0.1–0.4 mV/s. CV peak current values of (d) oxidation peak I_A, (e) reduction peak I_{C1}, and reduction peak I_{C2} for S@CN and S@Ni-CN versus square root of scan rate.

(GITT) [57]. The internal resistance (IR) of the cells was determined using the following equation:

$$IR = \frac{V_{QOCV} - V_{CCV}}{I_{(Applied)}} \tag{2}$$

where V_{QOCV} is the quasi-open-circuit voltage, V_{CCV} is the closed-circuit voltage, and $I_{(Applied)}$ is the applied discharge current density. As shown in Fig. S12, the S@Ni-CN based cell exhibited a noticeably smaller internal resistance than the S@CN based cell throughout the lithium sulfide decomposition process. This suggests that the Ni nanoparticles facilitate the decomposition of Li_2S by enhancing reaction kinetics and lowering the energy barrier of this step.

To check the specific capacity of the different electrodes, we conducted constant current charge-discharge (GCD) tests on both electrodes at 0.1C (Fig. 7a). All GCD curves displayed two discharge characteristics and one charging plateau, corresponding to the redox peak of the cyclic voltammetry curve. At 0.1 C, the S@Ni-CN electrode achieved a discharge specific capacity of 1319.2 mAh/g, which is higher than S@CN (1135.2 mAh/g), indicating that the S@Ni-CN has a higher sulfur utilization rate.

Fig. 7b and c shows the GCD curves of the S@CN and S@Ni-CN at different rates, respectively. It is apparent that with increasing charge and discharge currents, the discharge capacities of the battery gradually decrease, and the polarization degree of the electrode increases. At smaller charging and discharging rates, more obvious charging and discharging plateaus appeared for both the S@CN and S@Ni-CN; however, the latter had a flatter charging and discharging plateau and a higher capacity. When the applied current reached 2 C, the charging and discharging performance of the S@CN attenuated, leading to a significant decrease in battery capacity. This is because of the inability of lithium polysulfide to undergo fast conversion under higher currents, resulting in reduced battery capacity. In contrast, the S@Ni-CN still has an obvious charging and discharging characteristic, even at a higher rate, demonstrating that the addition of the Ni nanoparticles can increase the reactivity of the electrode and accelerate the decomposition speed of lithium sulfide, which can lead to greater discharge capacity

and improved cycling stability.

Fig. 7d shows a comparison of the overpotentials of the two electrodes at different current densities. From the figure, it is evident that the distance between the GCD curves increases with increasing current, and the distance represents the overpotential of the battery. The overpotential reflects the degree of internal polarization of the battery: a higher overpotential corresponds to a greater degree of internal polarization within the battery. Through comparison, it can be found that the overpotential of the S@CN is significantly higher than that of the S@Ni-CN, whether at high or small rates. When the C-rate goes up to 2 C, the overpotential of the S@CN reaches 0.63 V, which is much higher than that of the S@Ni-CN (0.38 V). This indicates that there is more polarization inside the battery, which means that the change between substances occurs more slowly. Additionally, this finding reveals that the addition of a Ni catalyst enhances the ability of the electrode to conduct electrochemical reactions, thereby accelerating the polysulfide conversion rate.

Fig. 7e shows a performance comparison between the S@CN and S@Ni-CN at 0.1, 0.2, 0.5, 1, and 2 C. From the graph, it can be seen that the first discharge-specific capacity of the S@Ni-CN reached 1319.2 mAh/g at 0.1C. As the current increased, the discharge capacity of the battery gradually decreased. When the applied rate reached 0.2 C, the discharge-specific capacity was 1049.1 mAh/g. With the current further increasing to 2 C, the battery capacity declined significantly, and the capacity of the S@Ni-CN was 532.3 mAh/g. The discharge rate was then reduced to 0.1C, and the discharge-specific capacity of the S@Ni-CN was restored to 1108.3 mAh/g. In contrast, the S@CN showed capacity of only 1138 mAh/g at 0.1C. As the current increased further, the decay rate of the battery capacity increased significantly. As the rate reached 0.2 C, the capacity of the cell was 987.5 mAh/g. However, With the current further increasing to 2 C, the discharge-specific capacity of the S@CN decreased to 387.6 mAh/g, which was much lower than that of the S@Ni-CN. After returning to 0.1C, the reversible capacity of the battery increased to 1015.4 mAh/g. In comparison, it is evident that the capacity efficiency of the S@Ni-CN surpasses that of the S@-CN, regardless of whether the rates are high or low.
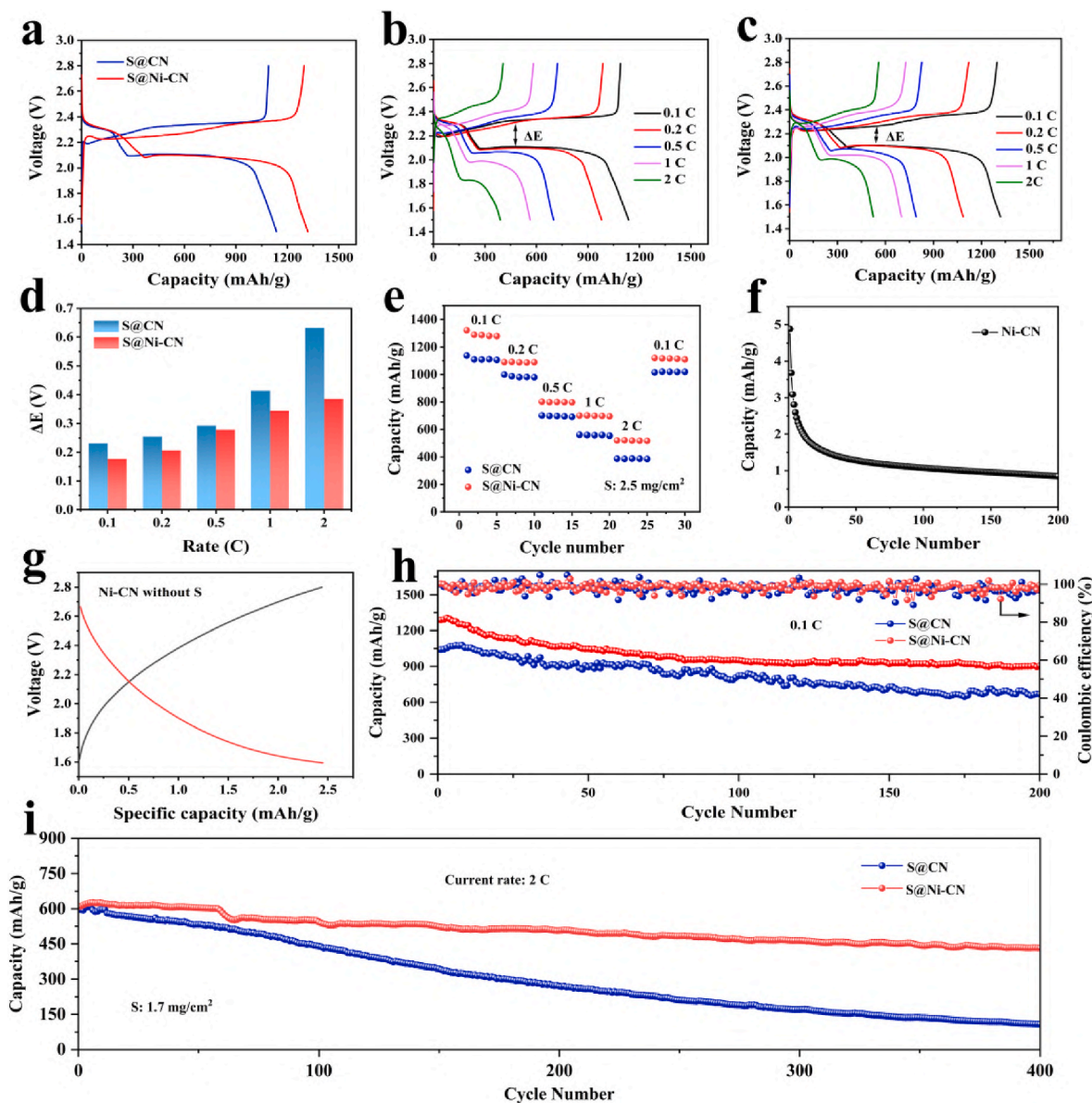
Fig. 7. (a) Charge-discharge curves of S@CN and S@Ni-CN electrodes at 0.1C. Charge-discharge curves of (b) S@CN and (c) S@Ni-CN at different C-rate. (d) The overpotential of S@CN and S@Ni-CN electrodes at different rates. (e) The comparison of C-rate performance between S@CN and S@Ni-CN. (f) Long cycle testing of Ni-CN without sulfur at a current of 0.1 mA. (g) Charge-discharge curve of Ni-CN without sulfur at a current of 0.1 mA. (h) Cycle performance of LSBs using the S@CN and S@Ni-CN at 0.1C. (i) Cycle performances of the S@CN and S@Ni-CN electrodes at 2 C.

Further, we conducted charge–discharge tests on the pure Ni-CN without sulfur loading at 0.1 mA (Fig. 7f and g), and it was observed that the contribution of the blank cathode to the battery capacity was very small and could be ignored. To further characterize the cyclic stability of the S@CN and S@Ni-CN materials, at 0.1C, we conducted 200 long-cycle tests on both electrodes. As displayed in Fig. 7h, the first discharge specific capacity of the S@Ni-CN was 1288.6 mAh/g. Following three activation cycles, the capacity reaches 1295.3 mAh/g. The S@Ni-CN demonstrated a more significant capacity decay in the first 26 cycles, after which the decay rate decreased. The reversible capacity after 200 cycles is 906.7 mAh/g. demonstrating a 70.4 % capacity retention and an average capacity degradation rate of merely 0.15 % per cycle. The mean coulombic efficiency was 98.2 %. By comparison, the S@CN exhibited an initial discharge-specific capacity of 1041.3 mAh/g at 0.1C. After seven activation cycles, the capacity increased to 1078.8 mAh/g. Following 200 cycles, the reversible capacity dropped to 694.6 mAh/g. The battery retained approximately 66 % of its original

capacity, and on average, its capacity decreased by 0.17 % per cycle. After 200 cycles at 0.5 C, the battery with S@Ni-CN still achieve a capacity of 586.1 mAh/g, with excellent capacity retention and better performance than the battery based on the S@CN (Fig. S13).

In addition, we tested the long-cycle durability of the cell at high current density to further evaluate its practical applications. Under a high current condition of 2 C, after 400 GCD cycles, the discharge capacity of S@Ni-CN remained at 433.4 mAh/g, showing an average capacity degradation of 0.07 % per cycle (Fig. 7i). This was superior to that of the S@CN (with a 0.2 % decrease in capacity per cycle). To further investigate the catalytic performance of nickel for different polysulfides at higher sulfur loadings (4.2 mg/cm²), we conducted cyclic voltammetry tests on two electrodes at 0.2 mV/s (Fig. S14), the CV of S@Ni-CN exhibited two distinct cathodic peaks at 2.28 (peak II) and 1.99 V (peak III), corresponding to the conversion of S into polysulfides and subsequently into insoluble Li_2S/Li_2S_2. In contrast, the pea III (2.51 V) was related to the oxidation process of Li_2S back to S. The S@CN based

battery shown smaller oxidation voltage (2.55 V) and higher reduction voltage (2.25 V, 1.66 V) at the same scanning rate, suggesting its effectiveness in promoting the electrochemical transformation of polysulfides.

Furthermore, the catalytic activities of the Ni nanoparticles, S@Ni-CN and S@CN electrodes were further evaluated base on the onset potential at which the current reached 10 μA cm^{-2} beyond the baseline (Fig. S14 and S15). According to Fig. S14d, the S@Ni-CN electrode displays comparatively higher onset potentials and smaller onset potentials, reflecting the minimal overpotential required for LiPSs reduction–oxidation process. This improved redox kinetics is mainly ascribed to the strong catalytic effect of Ni catalyst. Specifically, the d-band center of Ni lies close to the Fermi level and partially overlaps with the p-orbitals of sulfur atoms in lithium polysulfides, enabling strong electronic interactions and weakening S–S bonds. Additionally, Ni acts as a Lewis acid, forming Ni–S bonds through d-orbital coordination, thereby enhancing adsorption and activation of Li$_2$S$_x$ species. Long-chain polysulfides such as Li$_2$S$_6$ are adsorbed and destabilized on the Ni surface, while short-chain species like Li$_2$S$_2$ undergo S–S bond cleavage more readily. Furthermore, Ni forms a Ni–S interface with Li$_2$S, which lowers the decomposition overpotential and promotes its oxidation to elemental sulfur. These synergistic effects explain the reduced overpotential and enhanced catalytic performance observed in the S@Ni-CN electrode.

To examine the capacity performance of different cathodes at higher sulfur loading, the sulfur loading of the electrodes was increased to 4.2 mg/cm^2 and conducted 200 cycles at 1C (Fig. S16). The first discharge specific capacity of the S@Ni-CN was 613.4 mAh/g. Following 200 cycles, the reversible capacity remains at 458.8 mAh/g, maintaining 75 % of its initial capacity and exhibiting an average degradation rate of merely 0.13 % per cycle. In comparison, the S@CN exhibited an initial discharge-specific capacity of 452.2 mAh/g at 1 C. After 200 cycles, the reversible capacity decreased to 317.3 mAh/g. The capacity retained approximately 70.1 % of its original capacity, and on average, its capacity decreased by 0.15 % per cycle. This result further demonstrates the excellent catalytic ability of nickel nanoparticles towards polysulfide species.

The stability of electrode was assessed by disassembling the coin cell following the cyclic measurement. The FE-SEM images of S@Ni-CN demonstrated that the consistent particle structure of Ni-CN remained intact following 100 successive charge-discharge cycles (Fig.S17 c, d). The S@Ni-CN cathode exhibited a Li$_2$S layer following complete discharge, demonstrating the facile conversion of sulfur to Li$_2$S, thereby optimizing sulfur utilization. In addition, the stability of the nanostructure during the lithiation/delithiation process was demonstrated by comparing the original morphology of S@Ni-CN. This significant result was attributed to the excellent catalytic efficiency and effective adsorption performance of Ni-CN. To further demonstrate the enhancing effect of the S@Ni-CN on the reaction kinetics, we compared it with recently reported positive electrode materials and summarized the results in Table S1. The S@Ni-CN exhibits a lower capacity decay and a greater capacity than other electrode materials. The experimental results demonstrated an improved discharge capacity and enhanced cycling stability in LSBs using the S@Ni-CN.

4. Conclusion

In summary, metallic Ni was successfully compounded into MOF by a solvothermal method, and Ni-CN particles were prepared by high-temperature cracking. Ni-CN has an excellent conductivity, which is conducive to rapid electron migration, and the greater specific surface area and pore volume of Ni-CN can reveal more adsorption sites, accelerate the transformation of LiPSs, and thus achieve the purpose of inhibiting the shuttle effect. Most importantly, the introduction of a nickel catalyst promoted the transformation of LiPSs and lowered the potential barrier of the Li$_2$S decomposition reaction; thus, the S@Ni-CN

electrode had a more efficient kinetic conversion process. The electrochemical test results show that the initial discharge-specific capacity of the cell reaches 1288.6 mAh/g at 0.1C, and after 200 long cycles, its reversible capacity can still be remains at 906.7 mAh/g, with a capacity retention rate of 70.4 %, and the average capacity degradation rate of each cycle is only 0.15 %. Compared with the traditional porous carbon materials, this work embeds Ni nanoparticles in N- enriched porous carbon, which improves the adsorption capacity of LiPSs and enhances the redox reaction kinetics. This work presents a viable solution for the design of LSBs cathodes.

CRediT authorship contribution statement

Jixin Lu: Writing – original draft, Visualization, Validation, Methodology, Conceptualization. **Mengyuan Zhu:** Visualization, Methodology, Data curation. **MinSu Kim:** Formal analysis, Data curation. **Aihua He:** Software, Formal analysis. **Cunguo Wang:** Writing – review & editing, Supervision, Project administration, Conceptualization. **Tae Hyung Kim:** Writing – review & editing, Supervision, Data curation, Conceptualization. **Seung Hee Lee:** Writing – review & editing, Supervision, Project administration, Conceptualization.

Declaration of competing interest

No conflict of interest statement.

Appendix A. Supplementary data

Supplementary data to this article can be found online at https://doi.org/10.1016/j.jpowsour.2025.237269.

Data availability

Data will be made available on request.

References

[1] Z.K. Wang, Y. Li, H.Q. Ji, J.Q. Zhou, T. Qian, C.L. Yan, Unity of opposites between soluble and insoluble lithium polysulfides in lithium-sulfur batteries, Adv. Mater. 34 (47) (2022) 2203699, https://doi.org/10.1002/adma.202203699.

[2] Y. Jiang, H.Q. Liu, X.H. Tan, L.M. Guo, J.T. Zhang, S.N. Liu, Y.J. Guo, J. Zhang, H.F. Wang, W.G. Chu, Monoclinic ZIF-8 nanosheet-derived 2D carbon nanosheets as sulfur immobilizer for high-performance Lithium sulfur batteries, ACS Appl. Mater. Interfaces 9 (30) (2017) 25239–25249, https://doi.org/10.1021/acsami.7b04432.

[3] S.Y. Wang, Z.W. Wang, F.Z. Chen, B. Peng, J. Xu, J.Z. Li, Y.H. Lv, Q. Kang, A.L. Xia, L.B. Ma, Electrocatalysts in lithium-sulfur batteries, Nano Res. 16 (4) (2023) 4438–4467, https://doi.org/10.1007/s12274-022-5215-4.

[4] T.T. Sun, F.D. Huang, J.L. Liu, H. Yu, X.Y. Feng, X.F. Feng, Y. Yang, H.B. Shu, F.Q. Zhang, Strengthened d-p orbital-hybridization of single atoms with sulfur species induced bidirectional catalysis for lithium-sulfur batteries, Adv. Funct. Mater. 33 (51) (2023) 2306049, https://doi.org/10.1002/adfm.202306049.

[5] M.Y. Wang, Z.C. Bai, T. Yang, C.H. Nie, X. Xu, Y.X. Wang, J. Yang, S.X. Dou, N.N. Wang, Advances in high sulfur loading cathodes for practical lithium-sulfur batteries, Adv. Energy Mater. 12 (39) (2022) 2201585, https://doi.org/10.1002/aenm.202201585.

[6] X.Y. Yang, R. Li, J.X. Yang, H.Z. Liu, T. Luo, X.L. Wang, L. Yang, A novel route to constructing high-efficiency Lithium sulfur batteries with spent graphite as the sulfur host, Carbon 199 (2022) 215–223, https://doi.org/10.1016/j.carbon.2022.06.067.

[7] D.S. Jung, T.H. Hwang, J.H. Lee, H.Y. Koo, R.A. Shakoor, R. Kahraman, Y.N. Jo, M.S. Park, J.W. Choi, Hierarchical porous carbon by ultrasonic spray pyrolysis yields stable cycling in lithium-sulfur battery, Nano Lett. 14 (8) (2014) 4418–4425, https://doi.org/10.1021/nl501383g.

[8] J. Luo, X.F. Liu, W. Lei, Q.L. Jia, S.W. Zhang, H.J. Zhang, Self-standing lotus root-like host materials for high-performance lithium–sulfur batteries, Adv. Fiber Mater. 4 (6) (2022) 1656–1668, https://doi.org/10.1007/s42765-022-00206-y.

[9] D. Gueon, J.T. Hwang, S.B. Yang, E. Cho, K. Sohn, D.K. Yang, J.H. Moon, Spherical macroporous carbon nanotube particles with ultrahigh sulfur loading for lithium-sulfur battery cathodes, ACS Nano 12 (1) (2018) 226–233, https://doi.org/10.1021/acsnano.7b05869.

[10] Y.Y. Zhang, Z. Gao, N.N. Song, J.J. He, X.D. Li, Graphene and its derivatives in lithium-sulfur batteries, Mater. Today Energy 9 (2018) 319–335, https://doi.org/10.1016/j.mtener.2018.06.001.

[11] P.T. Liu, Y.Y. Wang, J.H. Liu, Biomass-derived porous carbon materials for advanced Lithium sulfur batteries, J. Energy Chem. 34 (2019) 171–185, https://doi.org/10.1016/j.jechem.2018.10.005.

[12] Z. Tao, J. Xiao, H. Wang, F. Zhang, Novel cathode structure based on spiral carbon nanotubes for lithium–sulfur batteries, J. Electroanal. Chem. 851 (2019) 113477, https://doi.org/10.1016/j.jelechem.2019.113477.

[13] R. Deng, B. Ke, Y. Xie, S. Cheng, C. Zhang, H. Zhang, B. Lu, X. Wang, All-solid-state thin-film lithium-sulfur batteries, Nano-Micro Lett. 15 (1) (2023) 73, https://doi.org/10.1007/s40820-023-01064-y.

[14] Y. Xia, R.Y. Fang, Z. Xiao, H. Huang, Y.P. Gan, R.J. Yan, X.H. Lu, C. Liang, J. Zhang, X.Y. Tao, W.K. Zhang, Confining sulfur in N-doped porous carbon microspheres derived from microalgaes for advanced lithium-sulfur batteries, ACS Appl. Mater. Interfaces 9 (28) (2017) 23782–23791, https://doi.org/10.1021/acsami.7b05798.

[15] Y.Y. Dong, D. Cai, T.T. Li, S. Yang, X.M. Zhou, Y.J. Ge, H. Tang, H.G. Nie, Z. Yang, Sulfur reduction catalyst design inspired by elemental periodic expansion concept for lithium-sulfur batteries, ACS Nano 16 (4) (2022) 6414–6425, https://doi.org/10.1021/acsnano.2c00515.

[16] K. Liu, H.M. Yuan, X.Y. Wang, P.Y. Ye, B.D. Lu, J.J. Zhang, W. Lu, F. Jiang, S. Gu, J.J. Chen, C.L. Yan, Y.Z. Li, Z.H. Xu, Z.G. Lu, Ultrafast strategy to fabricate sulfur cathodes for high-performance lithium-sulfur batteries, ACS Appl. Mater. Interfaces 15 (26) (2023) 31478–31490, https://doi.org/10.1021/acsami.3c04972.

[17] J.N. Wang, S.S. Yi, J.W. Liu, S.Y. Sun, Y.P. Liu, D.W. Yang, K. Xi, G.X. Gao, A. Abdelkader, W. Yan, S.J. Ding, R.V. Kumar, Suppressing the shuttle effect and dendrite growth in lithium-sulfur batteries, ACS Nano 14 (8) (2020) 9819–9831, https://doi.org/10.1021/acsnano.0c02241.

[18] J.W. Mu, H.L. Jiang, M. Yu, S.H. Gu, G.H. He, Y. Dai, X.C. Li, Thiophilic-lithiophilic hierarchically porous membrane-enabled full lithium-sulfur battery with a low N/P ratio, ACS Appl. Mater. Interfaces 14 (20) (2022) 23408–23419, https://doi.org/10.1021/acsami.2c03160.

[19] W.S. Hou, P.L. Feng, X. Guo, Z.H. Wang, Z. Bai, Y. Bai, G.X. Wang, K.N. Sun, Catalytic mechanism of oxygen vacancies in perovskite oxides for lithium-sulfur batteries, Adv. Mater. (Weinheim, Ger.) 34 (26) (2022) 2202222, https://doi.org/10.1002/adma.202202222.

[20] A. Chen, W.F. Liu, H. Hu, T. Chen, B.L. Ling, K.Y. Liu, Three-dimensional TiO₂-B nanotubes/carbon nanotubes intertwined network as sulfur hosts for high performance lithium-sulfur batteries, J. Power Sources 400 (2018) 23–30, https://doi.org/10.1016/j.jpowsour.2018.08.004.

[21] W.J. Dong, D. Wang, X.Y. Li, Y. Yao, X. Zhao, Z. Wang, H.E. Wang, Y. Li, L.H. Chen, D. Qian, B.L. Su, Bronze TiO₂ as a cathode host for lithium-sulfur batteries, J. Energy Chem. 48 (2020) 259–266, https://doi.org/10.1016/j.jechem.2020.01.022.

[22] F.Z. Chen, C.L. Sun, S.J. Robertson, S.Z. Chen, Y.H. Zhu, M.H. Shao, J.H. Wang, Unlocking robust lithium storage performance in high 1T-phase purity MoS₂ constructed by Mg intercalation, Nano Energy 104 (2022) 107894, https://doi.org/10.1016/j.nanoen.2022.107894.

[23] L. Tan, X.H. Li, Z.X. Wang, H.J. Guo, J.X. Wang, Lightweight reduced graphene oxide@MoS₂ interlayer as polysulfide barrier for high-performance lithium-sulfur batteries, ACS Appl. Mater. Interfaces 10 (4) (2018) 3707–3713, https://doi.org/10.1021/acsami.7b18645.

[24] S. Feng, J. Wang, J. Wen, X. Li, Z. Wang, Y. Zeng, J. Xiao, Improvement of redox kinetics of dendrite-free lithium–sulfur battery by bidirectional catalysis of cationic dual-active sites, ACS Sustain. Chem. Eng. 11 (23) (2023) 8544–8555, https://doi.org/10.1021/acssuschemeng.3c01158.

[25] S. Liao, Y. Xie, W. Zheng, Z. Huang, H. Zhang, Z.-Z. Luo, F. Zeng, C. Yang, S. Cheng, X. Wang, Enhancing rate performance in lithium-sulfur batteries via synergistic bidirectional catalysis and improved conductivity, Chem. Eng. J. (2025) 160022, https://doi.org/10.1016/j.cej.2025.160022.

[26] Y. Xie, W. Zheng, J. Ao, Y. Shao, X. Huang, H. Li, S. Cheng, X. Wang, Multifunctional Ni-doped CoSe₂ nanoparticles decorated bilayer carbon structures for polysulfide conversion and dendrite-free lithium toward high-performance Li-S full cell, Energy Storage Mater. 62 (2023) 102925, https://doi.org/10.1016/j.ensm.2023.102925.

[27] H. Zhang, W.Q. Zhao, M.C. Zou, Y.S. Wang, Y.J. Chen, L. Xu, H.S. Wu, A.Y. Cao, 3D, mutually embedded MOF@carbon nanotube hybrid networks for high-performance lithium-sulfur batteries, Adv. Energy Mater. 8 (19) (2018) 1800013, https://doi.org/10.1002/aenm.201800013.

[28] J. Chen, Y.J. Yang, S. Yu, Y. Zhang, J.W. Hou, N.F. Yu, B.Z. Fang, MOF-derived nitrogen-doped porous carbon polyhedrons/carbon nanotubes nanocomposite for high-performance lithium-sulfur batteries, Nanomaterials 13 (17) (2023) 2416, https://doi.org/10.3390/nano13172416.

[29] J. Park, S. Yoon, S. Oh, J. Kim, D. Kim, G. Kim, J. Lee, M.J. Song, I. Kim, K. Sohn, J. Kim, A systematic correlation between morphology of porous carbon cathode and electrolyte in lithium-sulfur battery, J. Energy Chem. 61 (2021) 561–573, https://doi.org/10.1016/j.jechem.2021.03.0362095-4956/.

[30] P.B.A. Geng, M. Du, X.T. Guo, H. Pang, Z.Q. Tian, P. Braunstein, Q. Xu, Bimetallic metal-organic framework with high-adsorption capacity toward lithium polysulfides for lithium-sulfur batteries, Energy Environ. Mater. 5 (2) (2022) 599–607, https://doi.org/10.1002/eem2.12196.

[31] Z.Q. Li, C.X. Li, X.L. Ge, J.Y. Ma, Z.W. Zhang, Q. Li, C.X. Wang, L.W. Yin, Reduced graphene oxide wrapped MOFs-derived cobalt-doped porous carbon polyhedrons as sulfur immobilizers as cathodes for high performance Lithium sulfur batteries, Nano Energy 23 (2016) 15–26, https://doi.org/10.1016/j.nanoen.2016.02.049.

[32] J. Wang, X. Chen, L. Chen, X. Li, J. Xiao, Wrapping ZIF-67 with vine-like carbon nanotubes to enhance the capture of polysulfide and consolidation of active site, J. Energy Storage 77 (2024) 109952, https://doi.org/10.1016/j.est.2023.109952.

[33] M. Xiang, J. Li, S. Feng, H. Zhang, X. Cao, Y. Zeng, X. Li, J. Xiao, Synergistic capture and conversion of polysulfides in cathode composites with multidimensional framework structures, J. Colloid Interface Sci. 624 (2022) 471–481, https://doi.org/10.1016/j.jcis.2022.05.118.

[34] W. Zhang, X. He, C. He, The "d-p orbital hybridization"-guided design of novel two-dimensional MOFs with high anchoring and catalytic capacities in Lithium−Sulfur batteries, J. Colloid Interface Sci. 678 (2025) 540–548, https://doi.org/10.1016/j.jcis.2024.08.184.

[35] H. Zhang, W.Q. Zhao, Y.Z. Wu, Y.S. Wang, M.C. Zou, A.Y. Cao, Dense monolithic MOF and carbon nanotube hybrid with enhanced volumetric and areal capacities for lithium-sulfur battery, J. Mater. Chem. A 7 (15) (2019) 9195–9201, https://doi.org/10.1039/c9ta00485h.

[36] M. Du, Q. Li, G.X. Zhang, F.F. Wang, H. Pang, Metal-organic framework-based sulfur-loaded materials, Energy Environ. Mater. 5 (1) (2022) 215–230, https://doi.org/10.1002/eem2.12170.

[37] H.Y. Lu, C. Zhang, Y.F. Zhang, Y.P. Huang, M.K. Liu, T.X. Liu, Simultaneous growth of carbon nanotubes on inner/outer surfaces of porous polyhedra: advanced sulfur hosts for lithium-sulfur batteries, Nano Res. 11 (12) (2018) 6155–6166, https://doi.org/10.1007/s12274-018-2130-9.

[38] J. Ao, Y. Xie, Y. Lai, M. Yang, J. Xu, F. Wu, S. Cheng, X. Wang, CoSe2 nanoparticles-decorated carbon nanofibers as a hierarchical self-supported sulfur host for high-energy lithium-sulfur batteries, Sci. China Mater. 66 (8) (2023) 3075–3083, https://doi.org/10.1007/s40843-022-2462-x.

[39] W. Zhang, S. Kong, W. Wang, Y. Cheng, Z. Li, C. He, Enhanced electrocatalytic performance of LCO-NiFe-C₃N₄ composite material for highly efficient overall water splitting, J. Colloid Interface Sci. 680 (2025) 787–796, https://doi.org/10.1016/j.jcis.2024.11.118.

[40] J. Zong, C. He, W. Zhang, Ultrafast carrier recombination in a BC₆N/SnXY Z-scheme heterostructure for water splitting: insights from ground-and excited-state carrier dynamics, J. Mater. Chem. A 12 (29) (2024) 18528–18536, https://doi.org/10.1039/d4ta02440k.

[41] C. He, Y. Liang, W. Zhang, Design of novel transition-metal-doped C₆N₂ with high-efficiency polysulfide anchoring and catalytic performances toward application in lithium–sulfur batteries, ACS Appl. Mater. Interfaces 14 (25) (2022) 29120–29130, https://doi.org/10.1021/acsami.2c07285.

[42] W. Zhang, X. He, C. He, The "dp orbital hybridization"-guided design of novel two-dimensional MOFs with high anchoring and catalytic capacities in Lithium−Sulfur batteries, J. Colloid Interface Sci. 678 (2025) 540–548, https://doi.org/10.1016/j.jcis.2024.08.184.

[43] Y. Xie, J. Cao, X. Wang, W. Li, L. Deng, S. Ma, H. Zhang, C. Guan, W. Huang, MOF-derived bifunctional Co₀.₈₅Se nanoparticles embedded in N-doped carbon nanosheet arrays as efficient sulfur hosts for lithium–sulfur batteries, Nano Lett. 21 (20) (2021) 8579–8586, https://doi.org/10.1021/acs.nanolett.1c02037.

[44] Z.X. Guang, Y. Huang, C. Chen, X.D. Liu, Z.P. Xu, W.J. Dou, Engineering a light-weight, thin and dual-functional interlayer as "polysulfides sieve" capable of synergistic adsorption for high-performance lithium-sulfur batteries, Chem. Eng. J. 383 (2020) 11, https://doi.org/10.1016/j.cej.2019.123163.

[45] C.G. Wang, H.W. Song, C.C. Yu, Z. Ullah, Z.X. Guan, R.R. Chu, Y.F. Zhang, L.Y. Zhao, Q. Li, L.W. Liu, Iron single-atom catalyst anchored on nitrogen-rich MOF-derived carbon nanocage to accelerate polysulfide redox conversion for Lithium sulfur batteries, J. Mater. Chem. A 8 (6) (2020) 3421–3430, https://doi.org/10.1039/c9ta11680j.

[46] J. Zhao, R.J. Pan, R. Sun, C.Y. Wen, S.L. Zhang, B. Wu, L. Nyholm, Z.B. Zhang, High-conductivity reduced-graphene-oxide/copper aerogel for energy storage, Nano Energy 60 (2019) 760–767, https://doi.org/10.1016/j.nanoen.2019.04.023.

[47] J.Y. Li, J.X. Jiang, Y.G. Zhou, M. Chen, S.H. Xiao, X.B. Niu, R. Wu, L. Yu, D.J. Blackwood, J.S. Chen, Nickel single-atom catalysts on porous carbon nanosheets for high-performance lithium-selenium batteries, Energy 285 (2023) 129434, https://doi.org/10.1016/j.energy.2023.129434.

[48] M.H. Sun, X.Z. Wang, Y. Li, Z.B. Zhao, J.S. Qiu, Selective catalytic oxidation of pollutant H₂S over Co-decorated hollow N-doped carbon nanofibers for high-performance Li-S batteries, Appl. Catal. B Environ. 317 (2022) 121763, https://doi.org/10.1016/j.apcatb.2022.121763.

[49] X. Cao, M.L. Wang, Y.L. Li, L. Chen, L.X. Song, W.L. Cai, W. Zhang, Y.Z. Song, Nitrogen balance on Ni-N-C promotor for high-energy lithium-sulfur pouch cells, Adv. Sci. 9 (33) (2022) 2204027, https://doi.org/10.1002/advs.202204027.

[50] Y. Bai, T.T. Nguyen, R. Chu, H. Song, N.H. Kim, J.H. Lee, Heterostructured TiN/TiO$_2$ on the hierarchical N-doped carbon for enhancing the polysulfide immobilization and sulfur reduction in lithium-sulfur battery, Chem. Eng. J. (Lausanne) 476 (2023) 146581, https://doi.org/10.1016/j.cej.2023.146581.

[51] J.S. Cai, Z.T. Sun, W.L. Cai, N. Wei, Y.X. Fan, Z.F. Liu, Q. Zhang, J.Y. Sun, A robust ternary heterostructured electrocatalyst with conformal graphene chainmail for expediting bi-directional sulfur redox in Li-S batteries, Adv. Funct. Mater. 31 (23) (2021) 2100586, https://doi.org/10.1002/adfm.202100586.

[52] Z.Q. Ye, Y. Jiang, L. Li, F. Wu, R.J. Chen, A high-efficiency CoSe electrocatalyst with hierarchical porous polyhedron nanoarchitecture for accelerating polysulfides conversion in Li-S batteries, Adv. Mater. 32 (32) (2020) 2002168, https://doi.org/10.1002/adma.202002168.

[53] Z.Y. Han, S.Y. Zhao, J.W. Xiao, X.W. Zhong, J.Z. Sheng, W. Lv, Q.F. Zhang, G.M. Zhou, H.M. Cheng, Engineering d-p orbital hybridization in single-atom metal-embedded three-dimensional electrodes for Li-S batteries, Adv. Mater. 33 (44) (2021) 2105947, https://doi.org/10.1002/adma.202105947.

[54] F.Y. Fan, W.C. Carter, Y.M. Chiang, Mechanism and kinetics of Li$_2$S precipitation in lithium-sulfur batteries, Adv. Mater. 27 (35) (2015) 5203–5209, https://doi.org/10.1002/adma.201501559.

[55] R. Chu, T.T. Nguyen, H. Song, P.M. Austeria, Y. Bai, D.H. Kim, J.H. Lee, N.H. Kim, Crystal transformation engineering for effective polysulfides blocking layer for excellent energy density lithium-sulfur batteries, Energy Storage Mater. 61 (2023) 102877, https://doi.org/10.1016/j.ensm.2023.102877.

[56] M.J. Shi, Z. Liu, S. Zhang, S.C. Liang, Y.T. Jiang, H. Bai, Z.M. Jiang, J. Chang, J. Feng, W.S. Chen, H.P. Yu, S.X. Liu, T. Wei, Z.J. Fan, A Mott-Schottky heterogeneous layer for Li-S batteries: enabling both high stability and commercial-sulfur utilization, Adv. Energy Mater. 12 (14) (2022) 2103657, https://doi.org/10.1002/aenm.202103657.

[57] F. Han, D. Yan, X. Guan, Q. Lu, S. Yin, Y. Yan, H. Zhou, P. Yang, Q. Zhang, S. Zhang, Self-assembled 3D CoSe-based sulfur host enables high-efficient and durable electrocatalytic conversion of polysulfides for flexible lithium-sulfur batteries, Energy Storage Mater. 71 (2024) 103652, https://doi.org/10.1016/j.ensm.2024.103652.